Energy Storage Materials 17 (2019) 211–219

Contents lists available at ScienceDirect

Energy Storage Materials

journal homepage: www.elsevier.com/locate/ensm

Atomistic insights into the reaction mechanism of nanostructured LiI: Implications for rechargeable Li-I_2 batteries

Zhixiao Liu[a], Xiong Pu[b], Fei Gao[a,c], Wangyu Hu[a,*], Huiqiu Deng[a,d,**]

[a] College of Materials Science and Engineering, Hunan University, Changsha 410082, China
[b] Beijing Institute of Nanoenergy & Nanosystems, Chinese Academy of Sciences, Beijing 10083, China
[c] Department of Nuclear Engineering and Radiological Sciences, University of Michigan, Ann Arbor, MI 48109, USA
[d] School of Physics and Electronic Science, Hunan University, Changsha 410082, China

ARTICLE INFO

Keywords:
Li-I_2 battery
LiI nanoparticle
Long-chain polyiodides
Nanoconfinement
First-principles approach

ABSTRACT

Using LiI nanoparticles as the active material is a promising way to improve the performance of the Li-I_2 battery. In this study, a first-principles approach is employed to reveal the reaction mechanism of an ultra-small LiI nanoparticle, represented by a $Li_{14}I_{14}$ cluster, with and without nanoconfined environment. This study is the first time to report that there are polyiodides longer than I_5^- as intermediate products. For the free $Li_{14}I_{14}$ cluster, the super-long polyiodides (I_{11}^- and I_{13}^-) are observed at the deep state of charge (delithiation). However, the super-long chains are converted to a compact I_{14} cluster at the end of delithiation process. The theoretical open circuit voltage between the I_{14} and $Li_{14}I_{14}$ clusters exhibits three plateaus. The highest plateau corresponds to the conversion between the compact I_{14} cluster and super-long chain-like polyiodides, and the wide medium-voltage plateau is attributed to the transmission between super-long chains and short chains. When the $Li_{14}I_{14}$ cluster is confined in a (14, 0) single wall carbon nanotube (weight ratio of LiI is 38%), the nanoconfined effect can change the cluster to one-dimensional LiI nanowire. The nanoconfined environment can eliminate the voltage plateau above 3 V, because the nanoconfined effect prohibits the formation of super-long polyiodides and the final charge products are $I_{x\,=\,2,\,3,\,5}$ molecules.

1. Introduction

Vehicle electrification and large-scale stationary energy storage urgently demand rechargeable batteries with high energy density, low cost and long service life [1–3]. Lithium-ion (Li-ion) batteries have acquired brilliant achievements since 1990s. However, cathode materials based on Li intercalation mechanism currently act as the bottleneck blocking the improvement of batteries' capacity and energy density [4]. In this regard, it is necessary to develop rechargeable Li batteries based on electrochemical conversion reaction mechanism [5–7].

Lithium-iodine (Li-I_2) batteries based on the conversion reaction between I_2 and LiI are promising next-generation energy storage devices due to the low fabrication cost, stable cyclability and decent energy density [8–11]. Comparing with lithium-sulfur (Li-S) batteries, the Li-I_2 system can deliver a high discharge voltage and achieve a faster reaction rate [12]. However, the shuttle effect, which impedes the commercialization of Li-S batteries, is also a crucial challenge for the practical application of rechargeable Li-I_2 batteries [13]. Aiming at improving the performance of Li-I_2 batteries, great efforts have been performed to alleviate the shuttle effect caused by the dissolution of I_2 and I_3^-. As with Li-S batteries, using nanostructured cathode hosts and surface decoration are effective approaches to prohibit the shuttle effect [14,15]. Ma and colleagues developed a nitrogen-doped graphene interlayer to prevent the migration of iodine species from the cathode side to the anode side [16]. Lu et al. reported that nitrogen and phosphorus co-doped graphitic carbon as the cathode host could improve the performance of the Li-I_2 battery, because heteroatoms could provide strong affinities to immobilize I_2 and I_3^- [11]. Zhao et al. found that nanoporous carbon can physically trap iodine species [9].

Another key challenge for fabricating iodine-based cathode is that iodine is sublimable at room temperature. To address this issue, LiI is employed to fabricate the cathode, because LiI exhibits higher melting and boiling points, which make heating accessible during fabricating the cathode [17]. As reported by Ref [17]., LiI imbedded into reduce graphene oxide (rGO) framework could still deliver 200 mA h/g capacity at 0.5 C after 100 cycles, and the hysteresis of the LiI@rGO cathode is smaller than 0.06 eV. Wu et al. synthesized meso-micro

* Corresponding author.
** Corresponding author at: School of Physics and Electronic Science, Hunan University, Changsha 410082, China.
E-mail addresses: wyuhu@hnu.edu.cn (W. Hu), hqdeng@hnu.edu.cn (H. Deng).

https://doi.org/10.1016/j.ensm.2018.07.016
Received 2 June 2018; Received in revised form 20 July 2018; Accepted 20 July 2018
Available online 26 July 2018
2405-8297/

porous carbon polyhedrons (MCP) as the cathode host for LiI nanoparticle, and found that LiI@MCP can achieve an excellent rate capability and stale cycling performance [18]. The LiI-based cathode can also be coupled with metal-free anodes to avoid safety issues caused by the Li dendrite growth [19].

The pioneering experimental investigations on LiI cathode pave a new way for improving the performance of Li-I_2 batteries. Inspired by knowledge from Li-S batteries, we believe that decreasing the size of active material nanoparticle to nanometers, even to the molecular scale, is a promising strategy to improve the cell performance [20,21]. In addition, a smaller nanoparticle size can enhance the charge transport kinetics [22,23]. Our current study is proposed to reveal how a sub-nanometer LiI nanoparticle behaves as the cathode active material in the Li-I_2 battery, and predict the electrochemical performance of such a small nanoparticle. In addition, the confinement effect on the ultra-small LiI nanoparticle is evaluated.

This study was proposed to use the *ab-initio* molecular dynamics simulation and density functional theory (DFT) analysis to unravel the reaction mechanisms of delithiating a LiI nanoparticle smaller than 1 nm. Theoretical simulation techniques have been widely used for understanding physiochemical properties of lithium polysulfides in Li-S battery cathodes. Using a first-principles approach, Zhang et al. predicted that polarized transition metal sulfides can provide strong affinity to polysulfides [24]. Liu et al. reported that silicene and Ti_2Si monolayer as cathode host materials not only can immobilize polysulfides but also facilitate reduction and dissociation of long-chain polysulfides to short chains [25,26]. Going beyond silicene and graphene, other monolayer materials including borophene, phosphorene and C_3B can also potentially serve as cathode host materials for suppressing polysulfide dissolution and adverse shuttle effect [27–29]. Mukherjee and collaborators predicted that solid Li_2S_2 exhibits much higher electronic conductivity than Li_2S [30]. Recently, Wang et al. successfully fabricated a Li-S battery based on Li_2S_2 and achieved high sulfur loading [31].

2. Results and discussion

In this study, we hypothesize that the Li_2S nanoparticle smaller than 1 nm is amorphous because the periodic atom arrangement can be destroyed at this length scale. In addition, previous studies on lithium peroxide (Li_2O_2) also demonstrated that the amorphous phase possessed faster charge transfer kinetics [32,33]. A recent study on sputter-deposited lithium sulfide also demonstrated that the amorphous Li_2S nanofilm as cathode material was more active than the crystalline Li_2S nanofilm in the Li–S battery [34].

The strategy to generate the nanoparticle was adopted from our previous study [35]:

(1) Employ the melt-and-quench approach [32] to generate amorphous LiI based on crystalline (3 × 3 × 3) LiI supercell as shown in Fig. 1.
(2) Generate a sphere with a radius of 0.5 nm at the center of the amorphous LiI, and remove atoms beyond the sphere. A $Li_{14}I_{14}$ cluster can be obtained at this step.
(3) Put the $Li_{14}I_{14}$ cluster in a 20 × 20 × 20 $Å^3$ cubic box. The cluster was roughly relaxed by AIMD at 300 K for 3 ps. After AIMD simulation, the cluster structure was then refined by DFT simulation.

It is worth noting that the final state of the $Li_{14}I_{14}$ cluster predicted by the present approach is not sensitive to the initial structure. According to our previous study on $Li_{20}S_{10}$ cluster, different initial structures will lead to the similar optimized structures with the same binding energies [35], and the binding energies also agree well with the binding energy of the $Li_{20}S_{10}$ structure predicted by CALYPSO [36].

The structure evolution of delithiating a free $Li_{14}I_{14}$ nanoparticle is demonstrated in Fig. 2. The strategy described below is employed to mimic the delithiation process:

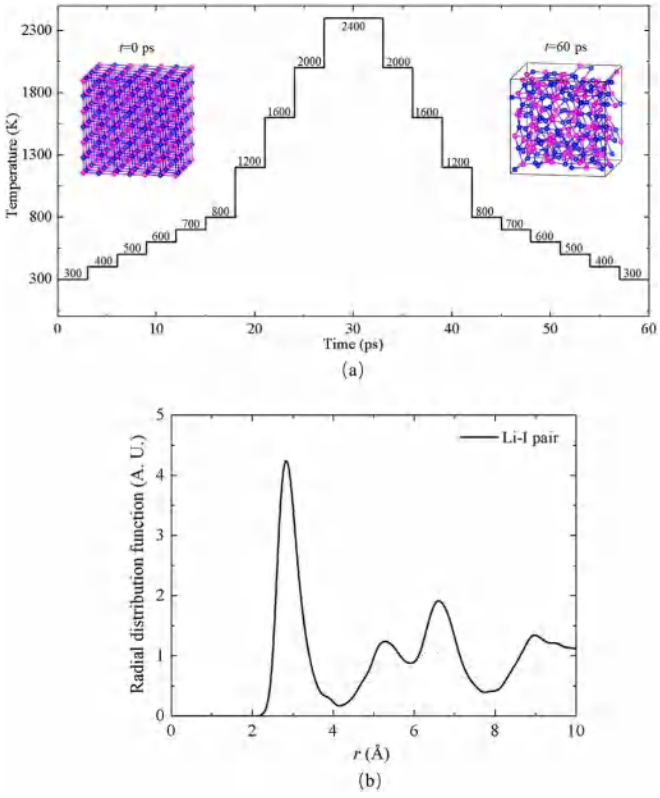

Fig. 1. (a) Temperature profile of the melt-quench strategy for generating amorphous LiI. Snapshots depict the structure of crystalline LiI at $t = 0$ ps and the structure of amorphous LiI at $t = 60$ ps. For $T <$ 2400 K, each simulation runs 3 ps. For T = 2400 K, the simulation runs 6 ps. (b) The radial distribution function of Li-I pair in amorphous LiI.

(i) Find four Li atoms which are the most far away from the mass center of the Li_xI_{14} cluster and remove two of them. We have six different combinations and we will get six $Li_{x-2}I_{14}$ clusters with different configurations.
(ii) Relax each cluster using AIMD at 300 K for 3 ps with a time step of 1.5 fs, and then optimize the structure using more accurate DFT simulations.
(iii) Pick up the $Li_{x-2}I_{14}$ cluster with the lowest total energy and repeat (i) and (ii).

To characters the morphological property of the cluster, the radius of gyration (R_g) of the cluster is also estimated as

$$R_g = \sqrt{\frac{\sum_i m_i r_i^2}{\sum_i m_i}}, \quad (1)$$

where m_i is the mass of the ith atom, and r_i is the distance of the ith atom to the mass center of the cluster.

For the $Li_{14}I_{14}$ cluster shown in Fig. 2(a), the radius of gyration is 4.55 Å. Given that the radius of the initial structure taken from amorphous is 5.5 Å, it can be inferred that the structure relaxation leads to a significant contraction. This phenomenon is also observed in our previous study about ultra-small Li_2S nanoparticle [35]. In crystalline LiI, each I atom coordinates with six Li atoms; In the $Li_{14}I_{14}$ cluster, however, each I atom only coordinates with three or four Li atoms. It is obvious that atoms are not fully coordinated, and dangling bonds can result in the contraction of the structure [37]. According to the present study, the Li–I bond length in the $Li_{14}I_{14}$ cluster is about 2.74 Å, which is about 0.16 Å shorter than the Li–I bond in the

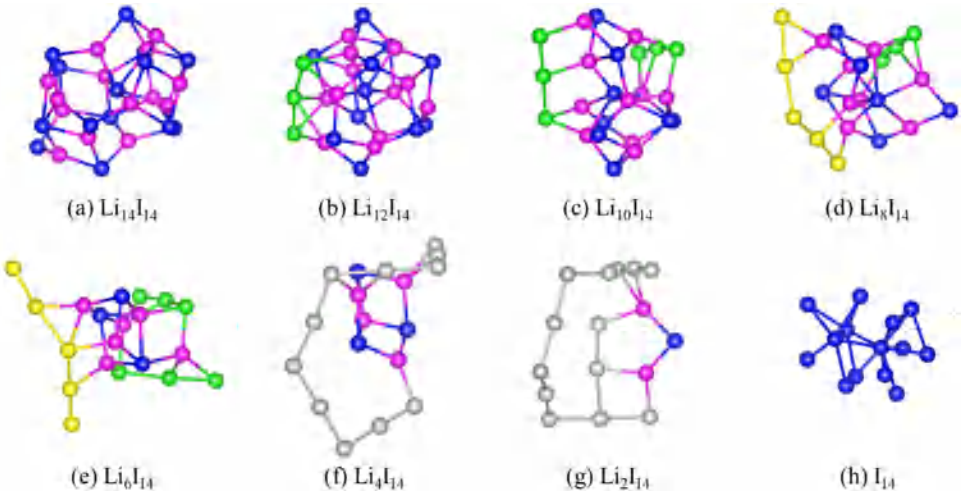

Fig. 2. The structure evolution during the delitiation process from the $Li_{14}I_{14}$ cluster to I_{14} cluster. The violet sphere represents the Li atom. The blue sphere represents the I atom which is either neutral or negatively charged by one electron. The green spheres represent I atoms in I_3 polyiodides. The yellow spheres represent atoms in I_5 polyiodides. Light gray spheres represent I atoms in I_x polyiodides with $x>5$.

amorphous LiI, and 0.26 Å shorter than the Li–I bond in crystalline LiI [38].

In the present study, the first delithiation step produces the $Li_{12}I_{14}$ cluster as shown in Fig. 2(b). It is interesting to find that the triiodide chain appears at the early stage of the delithiation process. The Bader charge analysis [39,40] is performed to estimate the ionic state of the trimer, and it is found that the trimer is negatively charged by 1 $|e|$ as I_3^-. Previous experimental studies have demonstrated that I_3^- is the only intermediate product between redox ends in Li-I_2 [9,16,41], Na-I_2 [42], K-I_2 [43], Mg-I_2 [44,45], Zn-I_2 [46], and Al-I_2 [47] batteries. According to our simulation, a free I_3^- chain exhibits the linear and symmetrical with a 2.97 Å bond length, which is a little shorter than the I_2 molecule [13,48]. However, in compounds, the form of I_3^- is dependent on the nature of cation [49]. For example, TlI_3 has the asymmetrical triiodide, in which two I–I bonds are 3.03 Å and 2.83 Å, and the bond angle is 177° [50]; but $KI_3{\cdot}H_2O$ has the symmetrical triiodide whose I–I bonds are both 2.93 Å [51]. In the $Li_{12}I_{14}$ cluster shown in Fig. 2(b), I_3^- is roughly symmetrical but not linear, in which I–I bonds are 2.93 Å and 2.95 Å with a bond angle of 169°. According to the molecular orbital theory, the extra electron should be localized at the antibonding orbital of the $5p_z$ pair from terminal I atoms. Bader charge analysis shows that the extra negative charge is evenly distributed to two terminal I atoms.

As shown in Fig. 2(c), another I_3^- appears in the $Li_{10}I_{14}$ cluster. It is interesting that the geometric symmetry of I_3^- decreases. In these two triiodides, the longer I–I bonds are 3.02 Å and 3.05 Å, and the shorter I–I bonds are 2.90 Å and 2.87 Å. According to the Bader charge analysis, it is interesting to find that the central I atom is always neutral whatever the symmetry of the I_3^- is. The extra negative charge evenly shared by two terminal I atoms when the polyiodide is symmetrical (Fig. 2(b)). For the asymmetrical I_3^-, the terminal I atom corresponding to the longer bond possesses more negative charge.

At the ~ 40% depth of charge (delithiation), a long polyiodide chain consisting of five I atoms in a "V" shape is observed in the Li_8I_{14} cluster. In the present study, the I–I bonds involving the central I atom are longer than bonds involving terminal I atoms. These fashions of I_5^- observed by the first-principle simulation agree well with the experimental measurements [49]. The formation of the long-chain I_5^- can be attributed to the oxidization of two I^- anions adjacent to a I_3^- anion as

$$I_3^- + 2I^- - 2e^- = I_5^-. \quad (2)$$

According to the Bader charge analysis, the extra negative charge mainly accumulates around the central atom and two terminal atoms of the I_5^- anion. It is worth noting that previous experimental studies proposed that I_3^- is the only intermediate product in metal-I_2 batteries [9,16,41–47]. Quite recently, Meng et al. developed a polyvinylpyrrolidone (PVP) cathode host as the I_2 host, and reported firstly that I_5^- is an intermediate product at the late stage of the first charge cycle and the initial stage of the second discharge cycle [52]. Our present simulation results strongly supported Meng et al.'s finding.

As the delithiation process goes (Fig. 2(e) to Fig. 2(g)), the I_5^- anion can merge with I_3^- and I^- ions, leading to forming a super-long polyiodide chain. The I–I bond length in the super-long chain varies from 2.85 Å to 3.06 Å. As the case of polyiodides shorter than I_5^-, the –1 $|e|$ charge is not evenly distributed to all iodine atoms. Snapshots in Fig. 2 demonstrate that polyiodides (I_3^-–I_{13}^-) always combine with LiI in the clusters via strong Li–I bonds. The previous theoretical prediction [35] and experimental study [53] also found this phenomenon in Li-S batteries based on nanostructure Li_2S cathodes.

At the end of the delithiation (charge) process, the super-long chain polyiodide shrinks to a compact I_{14} cluster (Fig. 2(h)) with a radius of gyration of 3.03 Å. The average I–I bond length in the I_{14} cluster is 2.72 Å, which is slightly longer than the bond of the free I_2 molecule, but shorter than the bonds of polyiodides predicted in the current study. Recently, Kim et al. synthesized a reduced graphene oxide (rGO)/LiI composite as cathode and found that the final charge product was I_2 [17]. It is worth noting that the I chemical potential for the I_{14} cluster ($\mu_I^{I_{14}}$) is around – 1.35 eV per I atom under zero-Kelvin first-principles condition; however, the theoretically calculated I chemical potential for the free I_2 molecule ($\mu_I^{I_2}$) is – 1.32 eV per I atom. It can be inferred that forming compact iodine cluster is energetically favored than forming I_2 molecules. The chemical potential for I in the infinite-large crystalline bulk (μ_I^{bulk}) is – 1.45 eV per atom, which is lower than the other two cases. However, for a crystalline iodine particle, specific surface area always increases with decreasing the particle size, which leads to many dangling bonds as well as high surface energy. Transferring crystalline structure to the condense amorphous structure can make an atom coordinate with more atoms and lower the energy of the system.

The delithiation process of the ultra-small LiI nanoparticle is quite different from that of the Li_2S nanoparticle. During the delithiation process, the polyiodide chain continually grows longer, and the chain becomes cluster as the final product as shown in Fig. 2(h). However, for the ultra-small Li_2S nanoparticle, the final product is the cyclo-ring. Also, the local disproportionation and reduction reactions, which shorten the length of polysulfides, occurs during the delithiation process although the entire delithiation process is an oxidization reaction for sulfur species [35].

The radius of gyration as the function of Li content is plotted in

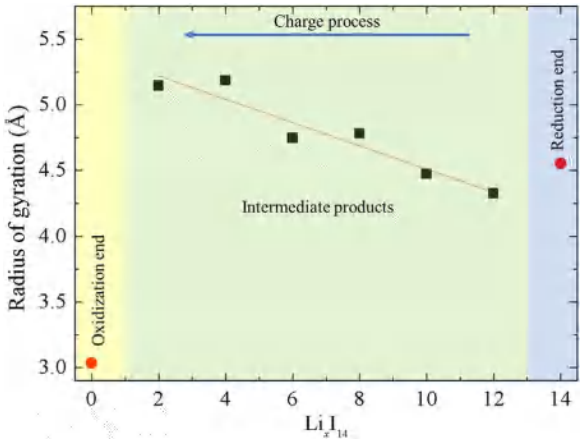

Fig. 3. The evolution of the radius of gyration during the delithiation (charge) process.

Fig. 3 for charactering the evolution of the cluster morphology during the delithiation process. Beyond the redox ends, the intermediate products exhibit a negative delithiation-induced compaction rate (lithiation-induced expansion rate). This trend is oppositely to the delithiation of an ultra-small Li_2S nanoparticle. According to our previous theoretical study, the radius gyration of the Li_xS_{10} cluster tends to decrease as the number of Li atom decreases [35]. As shown in Fig. 3, the radius of gyration of the oxidization end I_{14} drops significantly due to the phase transition of super-long chain to the compact cluster.

Previous theoretical studies on Li_2S and Li_2O_2 showed that although their bulk phases acted as insulator, their surface states exhibited metallic properties [54,55]. As the particle size decreases, the specific surface area increases significantly. In addition, the nanoparticle considered in the present is amorphous. Disordering lattice sites may also change the electronic structure. Fig. 4 depicts density of states of Li_xI_{14} clusters with different Li content. It is found that these clusters still act as insulators for electron transfer.

In previous studies on metal-I_2 batteries, only I_3^- was identified as the intermediate product by Raman analysis. Recently, Meng *et al.* detected I_5^- anion using in-situ Raman analysis when studying the reaction mechanism of a PVP-I_2 cathode [52]. They found that the

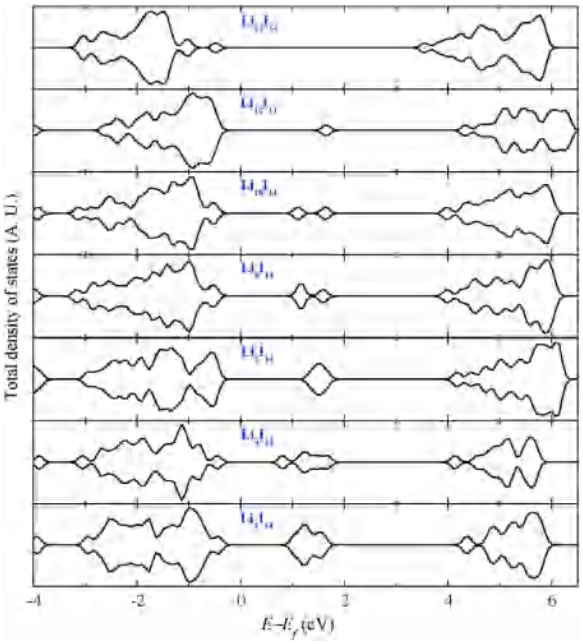

Fig. 4. Total density of states Li_xI_{14} clusters.

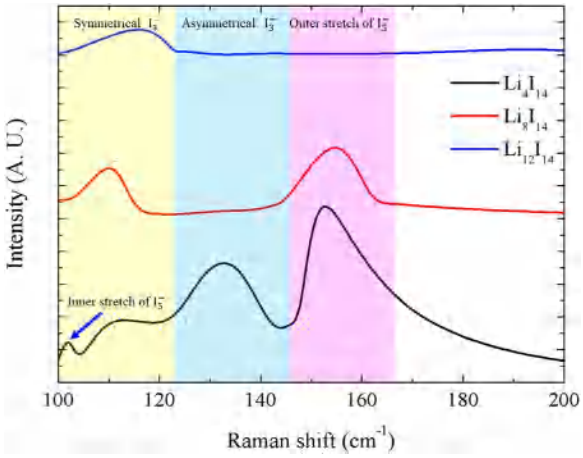

Fig. 5. Raman spectra of $Li_{12}I_{14}$, Li_8I_{14} and Li_4I_{14} predicted by the current theoretical calculations.

strong attractive interaction between I_5^- and PVP is helpful for stabilizing this long polyiodide. In earlier experimental studies on metal-I_2 batteries, graphitic carbon-based materials were usually used as cathode host materials. Graphitic carbon cannot prohibit the dissolution of long polyiodides into the organic electrolyte. The dissolved long polyiodides are not stable and can dissociate to I_3^- and I_2 in organic electrolyte systems.

Fig. 5 depicts the Raman spectra of $Li_{12}I_{14}$, Li_8I_{14} and Li_4I_{14} calculated by the vasp_raman.py code developed by Fonari and Stauffer [56]. $Li_{12}I_{14}$ only has one peak located between 100 cm^{-1} and 120 cm^{-1}, which is related to the symmetrical I_3^- [57]. As shown in Fig. 2(d), the Li_8I_{14} cluster has I_3^- and I_5^-. In the Raman spectra for Li_8I_{14}, we can also observe the peak between 100 cm^{-1} and 120 cm^{-1}, which represents the I_3^- anion. Another peak in the Raman spectra of Li_8I_{14} is located between 140 cm^{-1} and 160 cm^{-1}. This peak is from the outer stretch vibration of the bent I_5^- as reported by Nour et al. [57]. Fig. 2(f) clearly shows that Li_4I_{14} has a polyiodide chain with 11 I atoms. According to Nour et al.'s opinion, I_{11}^- can be treated as the combination of a pentaiodide and two triiodides. By comparing the current theoretical spectra of Li_4I_{14} with Nour et al.'s result, it can be inferred that the small peak located around 102 cm^{-1} is contributed by the inner stretch vibration of bent pentaiodide. In addition, the peak around 130 cm^{-1} is attributed to the asymmetrical triiodide.

The formation energies of intermediate products are calculated respecting to redox ends as [58]:

$$E_f = E_{Li_xI_{14}} - \frac{1}{14}(xE_{Li_{14}I_{14}} + (14-x)E_{I_{14}}). \quad (3)$$

Here, $E_{Li_{14}I_{14}}$, $E_{I_{14}}$ and $E_{Li_xI_{14}}$ are energies of $Li_{14}I_{14}$, I_{14} and intermediate products, respectively. The formation energies are plotted in Fig. 6(a). The species located at the convex hull is thermodynamically stable and will not decompose [59]. By assuming the discharge (lithiation) process and charge (delithiation) process experience the same intermediate products, the open circuit voltage (OCV) profile versus metallic Li anode can be estimated as [60]:

$$U = -\frac{E_{Li_yI_{14}} - E_{Li_xI_{14}} - (y-x)\mu_{Li}}{y-x}, \quad (4)$$

where μ_{Li} is the energy of a Li atom in the body-centered cubic phase. As shown in Fig. 6(b), the profile exhibits three plateaus. LiI-embedded porous carbon [18] and rGO/LiI composite [17] were tested as cathode materials for Li-I_2 batteries, and both of these studies demonstrated that the voltage profiles of LiI-based cathodes go through three stages during the charge or discharge cycles. To clearly elucidate the relation between the voltage and polyiodides, we go through the profile shown in Fig. 6(b) from the I_{14} state to $Li_{14}I_{14}$ state. The voltage profile starts

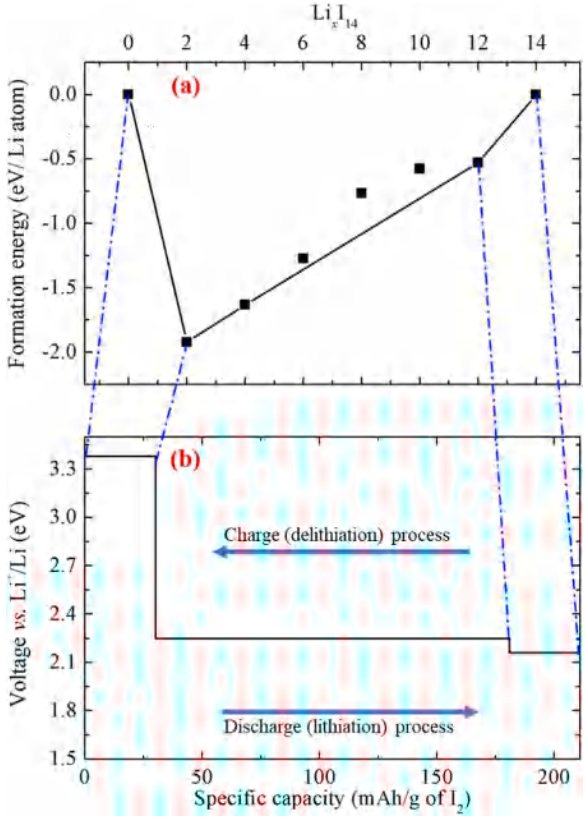

Fig. 6. (a) Formation energies of Li_xI_{14} clusters respecting to the Li_{14}. (b) Theoretically predicted open circuit voltage *vs.* Li^+/Li.

with the highest plateau of 3.38 V, which corresponds to the phase transition from the compact I_{14} to the super-long chain-like Li_2I_{14}. By revisiting Fig. 2, we can find that the long-chain polyiodides are gradually reduced to I_3^- and I^- anions in the second plateau, and the long-to-short polyiodide conversion makes a main contribution to the voltage profile. At the end of the discharge process, all anions are reduced to I^-, which gives the lowest plateau of 2.16 V. In general, the following reaction equations can be used to describe the discharge process:

$$I_{14}+2Li^+ +2e^- = LiI + LiI_{13},\ U = \quad 3.38V$$

$$LiI_{13}+10Li^+ +10e^- = LiI_3+10LiI,\ U = \quad 2.25V$$

$$LiI_3+2Li + 2e^- = 3LiI,\ U = \quad 2.15V$$

Recently, Meng et al. fabricated a Li-I_2 battery with polyvinylpyrrolidone-iodine (PVP-I_2) composite as cathode material, and three-plateau voltage profile was also observed [52]. They reported that the highest voltage was attributed to the formation of long-chain I_5^-. In Li-S batteries, according to both modeling analysis [61] and experimental studies [62], the highest plateau also corresponds to conversion of solid S_8 to long-chain lithium polysulfides; then the reactions producing short polysulfides leads to the second plateau; and finally discharge reactions stop at the formation of Li_2S. During the charge process, these three stages appear reversely [63,64]. The theoretical energy density based on the OCV shown in Fig. 6(b) is 506 Wh/kg, which is lower than the theoretical energy density of $LiFePO_4$ (600 Wh/g) and $Li_3Mo_{0.5}V_{1.5}(PO_4)_3$ (654 Wh/g) [65]. Biasi *et al.* measured the gravimetric energy densities of a series of $LiNi_mMn_nCo_{(1-m-n)}O_2$, and found that the energy densities are always above 550 Wh/kg [66]. In the term of energy density, the ultra-small LiI nanoparticle has less competitiveness than the intercalation-based cathode materials mentioned above. However, LiI-based Li-I_2 batteries are still applicable for large-scale stationary energy storage due to the low cost.

It is worth noting that the theoretical OCV of the ultra-small LiI nanoparticle is about 0.5 V lower than the discharge voltages reported by Kim et al. [17] and Wu et al. [18] In Li-S batteries, it has also been observed that the predominant plateau in the voltage profile drops down with reducing the particle size of active materials. Usually, the voltage of the Li-S battery is around 2.2 V [67]. Meng et al. deposited an amorphous Li_2S nanofilm on the copper foil, and found that the discharge voltage was only about 1.7 V but good rate capability was achieved [68]. Xin et al. found that the small sulfur allotropes (*i. e.* S_2–S_4) embedded into the micro-porous carbon only delivered a voltage of 1.9 V [69]. Our previous theoretical study also found that the equilibrium voltage corresponding to conversion reactions between nanostructured Li_2S and S was 0.3 V lower than that between bulk Li_2S and α-S [35,70].

Previous theoretical studies demonstrated that hole polarons can potentially serve as charge carriers in solid discharge products of metal-air batteries [32,71–77]. Recent theoretical study also showed that hole polarons are helpful for increasing the electronic conductivity of crystalline S [78], Li_2S_2 [30], L_2S [70] and Li_xS_{10} clusters [35]. Luntz *et al.* also reported that hopping of hole polarons in the discharge products affected the practical current densities [79].

In the current study, Heyd–Scuseria–Ernzerhof (HSE06) [80] hybrid functional is used to investigate polaron distribution in Li_xI_{14} clusters. Previous studies showed that electron polarons were less stable than hole polarons in crystalline Li_2S [70] as well as Li_2S_2 [30], amorphous Li_2S nanoparticle [35], and crystalline Li_2O_2 [81]. Following our previous study, it is hypothesized that two hole polarons will form first before removing Li ions from the cluster at each delithiation step [35].

The polarized $Li_{14}I_{14}$ cluster is produced by removing two electrons from the cluster, which is equivalent to introducing two positive charges. According to the current study, the magnetic moment of polarized $Li_{14}I_{14}$ is 2 μ_B. Fig. 7(a) shows the spin density of in the polarized $Li_{14}I_{14}$ cluster. It is found that each polaron is shared by two I atoms. According to the Bader charge analysis, each I atom is charged by – 0.5 $|e|$. Hence, the polaron is located at an iodine dimer as I_2^-. The I-to-I distance related to the polaron is around 3.2 Å, which is almost 0.6 Å longer than the bond length of the free I_2 molecule. If we revisit the Fig. 2(b), it is interesting to found that I_2^- is the precursor of the I_3^-. After the polarized $Li_{14}I_{14}$ lost two Li^+, one I_2^- will combine with an I^- anion to form I_3^-:

$$I_2^- + I^- = I_3^- + e^-. \quad (5)$$

This local reaction will produce a negative charge, which will reduce the other I_2^- to two I^- anions:

$$e^- + I_2^- = 2I^-. \quad (6)$$

Hence, this process yields the charge conservation:

$$2I_2^- = I_3^- + I^-. \quad (7)$$

For the polarized $Li_{12}I_{14}$ cluster (Fig. 7(b)), one hole polaron is localized at the triiodide, which makes the trimer neutral; and the other is shared by two I atoms, which is similar to the polaron in $Li_{14}I_{14}$. Comparing Fig. 7(b) and Fig. 2(c), it can be found that the I_2^- anion in the polarized $Li_{12}I_{14}$ is still the precursor of the I_3^-. For the polarized $Li_{10}I_{14}$ cluster (Fig. 7(c)), one polaron exists in a form of I_2^-, and the other one is localized at a triiodide. Also, comparing Fig. 7(c) and Fig. 2(d), it can be found that the I_2^- anion can bind with its adjacent I_3^- anion, resulting in forming a I_5^- anion. Fig. 7(d) depicts the spin density distribution in the polarized Li_8I_{14} cluster. One polaron makes the original I_5^- anion be neutral, and the other hole polaron is still existed as I_2^- which will be converted to I_3^- in Li_6I_{14} (Fig. 2(e)). For Li_xI_{14} with $x \leq 6$, introducing polarons to the cluster will dissociate the long chain to short chains as shown in Fig. 7(e)–(g). For these polarized clusters, the dissociated chains will recombine after removing Li^+ cations.

Li/Na-X (X = S, Se, I) batteries based on the conversion reaction

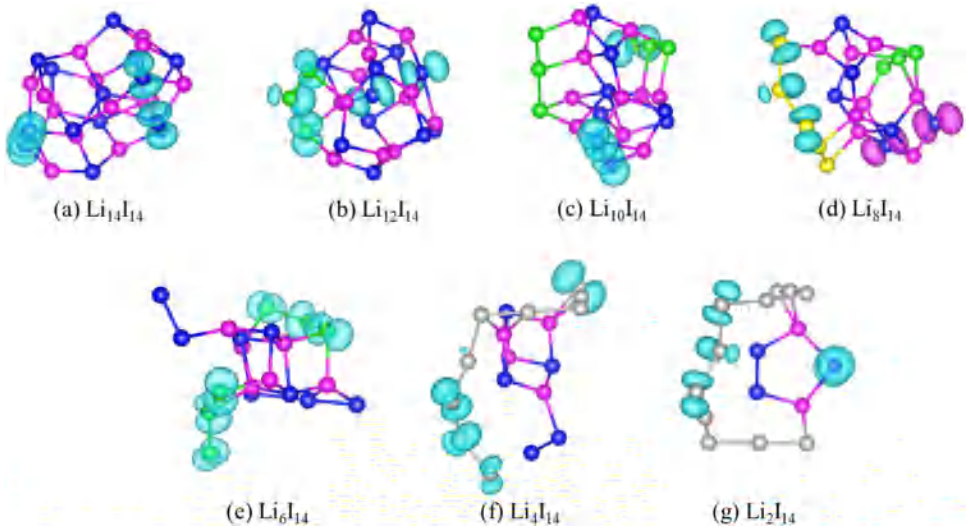

Fig. 7. Spin density distribution in the Li_xI_{14} cluster polarized by two hole polarons. The cyan isosurface represents spin-up states and the violet isosurface represent the spin-down states.

mechanism usually use confined structures to prohibit the shuttle effect [18,42,69,82]. In this study, we also investigated the $Li_{14}I_{14}$ confined in a single wall carbon nanotube ($Li_{14}I_{14}$@SWCNT). The $Li_{14}I_{14}$ cluster is confined in a (14, 0) SWCNT repeated four periods along the *Z* direction (256 C atoms totally). The weight ratio of LiI to C is as high as 38%, which is close to 30 wt% LiI in microporous carbon reported by Wu et al. [18] The diameter of the (14, 0) SWCNT is 1.1 nm, and SWCNTs in adjacent images are separated by 20 Å in *X* and *Y* directions. The length of the SWCNT in the supercell is 17.04 Å.

Fig. 8(a) shows the optimized $Li_{14}I_{14}$ in the (14, 0) SWCNT. In the nanoconfined environment, the $Li_{14}I_{14}$ clusters in adjacent images along *Z* direction merge with each other and form the one-dimensional (1D) LiI nanowire. For the confined LiI nanowire, the average Li–I bond length is 2.74 Å, which coincides with the Li–I bond length in the $Li_{14}I_{14}$ cluster.

Based on the structure of $Li_{14}I_{14}$ shown in Fig. 8(a), four different $Li_{12}I_{14}$ structures are generated and the one with lowest energy is depicted in Fig. 8(b). In the $Li_{12}I_{14}$@SWCNT, I species sill remain as I^- anions. Compared with $Li_{14}I_{14}$@SWCNT, the average Li–I bond length is slightly increased to 2.79 Å. As shown in Fig. 8(c), I_3^- exists when the active material is delihitated to $Li_{10}I_{14}$. More I_3^- anions continually appear as the delithiation process goes to Li_6I_{14}@SWCNT, as shown in Fig. 8(d)-(e). pentaiodide and hexaiodide appear in Li_4I_{14}@SWCNT (Fig. 8(f)). According to the Bader charge analysis, the V-shaped pentaiodide is negatively charged by 1 $|e|$ as I_5^-, and the linear-like hexaiodide is negatively charged by 1.8 $|e|$. In Li_2I_{14}@SWCNT (Fig. 8(g)), the hexaiodide chain is oxidized and only negatively charged by 0.15 $|e|$. In addition, triiodide chain and tetraiodide chain are also observed in Li_2I_{14}@SWCNT, whose ionic states are both − 1. In other words, the products at late charge state are not neutral but

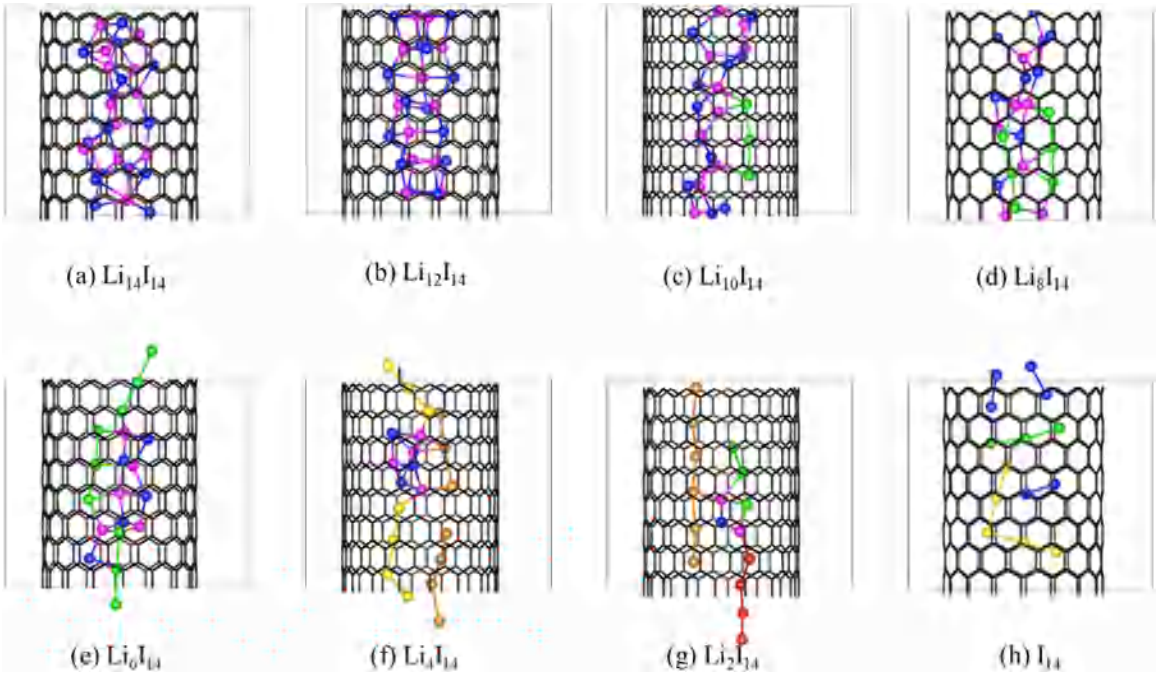

Fig. 8. The structure evolution of delithiating $Li_{14}I_{14}$ confined in a (14, 0) SWCNT. Violet spheres represent Li atoms. Blue spheres represent I atoms which are either neutral or negatively charged by one electron. The green spheres represent I atoms in I_3 polyiodides. Red spheres represent I atoms in I_4 polyiodides. The yellow spheres represent atoms in I_5 polyiodides. Orange spheres represent I atoms in I_x polyiodides with $x>5$.

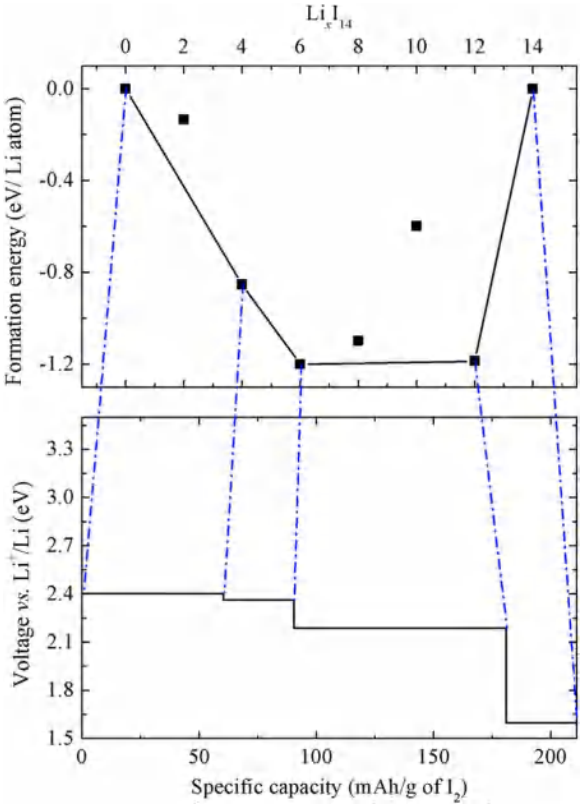

Fig. 9. (a) Formation energies of Li_xI_{14} confined in (14, 0) SWCNT. (b) Theoretically predicted open circuit voltage *vs.* Li^+/Li.

negatively charged, and the negative charge is from the SWCNT container.

In this nanoconfined environment, the final delithiation (charge) products are I_x (x = 2, 3, 5) chains rather than an integrated and compact cluster-like structure Fig. 8(h). For the shortest I_2 molecules confined in the (14, 0) SWCNT, the bond lengths are 2.75–2.81 Å, which are slightly longer than the free I_2 molecule. Each atom of the confined I_2 molecules is negatively charged by about 0.1 $|e|$, and increase in the bond length is attributed to the electrostatic repulsion between coupled I atoms. The I_3 molecule is symmetrical, and two bonds are 2.90 Å. The I_3 molecule is also negatively charged, and each terminal I atom has − 0.20 $|e|$ charge. In addition, the V-shaped I_5 molecule is also negatively charged by 0.61 $|e|$. The charge transfer from the SWCNT wall to I_x molecules indicates that there are chemical interactions between the carbon framework and iodine species. Li et al. [83] investigated the chemical and geometrical features of sulfur encapsulated in SWCNTs with a diameter of 1 nm, and found non-bonded interactions between sulfur and the wall. They also found that the small S_2 molecules will polymerize to form helix sulfur chain. Fujimori et al. also reported that the 1D linear and zigzag sulfur chains could be stabilized in narrow SWCNTs, and the sulfur chains exhibit good electronic conductivity [84].

Based on Eqs. (3) and (4), we calculate the formation energies of intermediate products and the related theoretical OCV profile of lithium iodide confined in SWCNT. Compared with the free $Li_{14}I_{14}$ nanoparticle, it can be found that the nanoconfinement effect can erase the voltage plateau above 3.3 V (Fig. 9). The reason is that the discharge process starts at the reduction of I_{2-5} molecules rather than the conversion of solid iodine to super-long polyiodides. As discussed above, the highest plateau in Fig. 6(b) is related to the conversion between compact I_{14} cluster and the super-long lithium polyiodides. Zhao et al. developed a Li-I_2 battery with aqueous cathode. In their particular battery, the active material is I_3^- dissolved in the aqueous electrolyte, and the I_3^-/I^- redox couple only leads to a single plateau in the voltage profile [85]. In the Li-S battery developed by Xin et al., [69] the discharge voltage also only has a wide single plateau because the unique nature of small sulfur allotropes can avoid the conversion of solid sulfur to long-chain polysulfides.

3. Conclusion

In this study, a first-principles approach is employed to reveal the reaction mechanisms of ultra-small LiI nanoparticle, represented by a $Li_{14}I_{14}$ cluster, as the active material for the Li-I_2 battery. For the free $Li_{14}I_{14}$ cluster, it is interesting found that the long-chain polyiodides $I_{x\geq5}^-$ appear at the deep state of charge (delithiation), but polyiodides are converted to an amorphous and compact iodine cluster as the final charge product. A three-plateau OCV profile is predicted based on the energy of Li_xI_{14} clusters with different Li content. The highest 3.38 V plateau is attributed to the conversion between iodine nanoparticle and the super-long chain-like lithium polyiodides, the medium 2.25 V plateau is caused by the conversion between long chains to short chains, and the lowest 2.16 V plateau represent forming stoichiometric LiI nanoparticle.

The effect of nanoconfinement on the reaction mechanism of LiI is also thoroughly investigated in this study. it is found that the $Li_{14}I_{14}$ cluster can be converted to LiI nanowire when confined in a (14, 0) SWCNT. In this nanoconfined environment, the length of the intermediate product cannot exceed I_6, and the final product is I_x molecules with x = 2, 3, 5. The nanoconfinement can eliminate the plateau above 3 V, because the charge/discharge process does not undergo the conversion between the compact iodine cluster and long-chain polyiodides.

4. Computational details

All simulations in this study were performed on Vienna *Ab-initio* Simulation Package (VASP) [86,87] based on the density functional theory (DFT) [88,89]. The projector augmented-wave (PAW) method [90] was employed for description the ion-electron interactions and the Perdew–Burke–Ernzerhof (PBE) functional [91] was used to describe the electron-electron exchange correlations. All *ab-initio* molecular dynamics (AIMD) simulations were carried out using NVT ensemble with the 300 eV energy cutoff of plane wave basis sets and 1.5 fs time step. The Nosé-thermostat [92] with a mass of ~ 50 amu Å^2 (SMASS = 0.30) [32] was used to control the temperature oscillation. The purpose of the AIMD simulation with small cutoff energy was conducting the relatively rough structure relaxation. After the AIMD simulation, the DFT simulation with 400 eV cutoff energy was conducted to accurately optimize atom positions, and the residual force for relaxing was set to 0.02 eV/Å. For all DFT simulations and AIMD simulations, spin polarization was considered and only Γ-point was sampled in the first Brillouin zone. Since the PBE-level functional always underestimated the electron localization, Heyd–Scuseria–Ernzerhof (HSE06) [80] hybrid functional with α = 0.5 was used for polaron simulation.

Acknowledgements

This work is financially supported by National Natural Science Foundation of China (Grant no.: 51771073). The authors thank National Supercomputing Center in Changsha for computing resources. Z. Liu would like to thank the Fundamental Research Funds for the Central Universities. The valuable suggestion for Raman analysis from Dr. M. Chen at Hunan University is greatly appreciated.

References

[1] M. Armand, J.M. Tarascon, Building better batteries, Nature 451 (2008) 652–657.
[2] J. Fjelstul, Vehicle electrification: on the “green” road to destination sustainability, J. Destin. Mark. Manag. 3 (2014) 137–139.

[3] B. Dunn, H. Kamath, J.M. Tarascon, Electrical energy storage for the grid: a battery of choices, Science 334 (2011) 928–935.
[4] V. Etacheri, et al., Challenges in the development of advanced Li-ion batteries: a review, Energy Environ. Sci. 4 (2011) 3243–3262.
[5] J. Cabana, et al., Beyond intercalation-based Li-Ion batteries: the state of the art and challenges of electrode materials reacting through conversion reactions, Adv. Mater. 22 (2010) E170–E192.
[6] P.G. Bruce, et al., Li-O-2 and Li-S batteries with high energy storage, Nat. Mater. 11 (2012) 19–29.
[7] J. Xu, et al., Recent progress in the design of advanced cathode materials and battery models for high-performance lithium-X (X = O-2, S, Se, Te, I-2, Br-2) batteries, Adv. Mater. 29 (2017) 1606454.
[8] Y. Wang, et al., Rechargeable lithium/iodine battery with superior high-rate capability by using iodine–carbon composite as cathode, Energy Environ. Sci. 4 (2011) 3947–3950.
[9] Q. Zhao, et al., Rechargeable lithium-iodine batteries with iodine/nanoporous carbon cathode, Nano Lett. 15 (2015) 5982–5987.
[10] K. Li, et al., Anchoring iodine to N-doped hollow carbon fold-hemisphere: toward a fast and stable cathode for rechargeable lithium–iodine batteries, ACS Appl. Mater. Interfaces 9 (2017) 20508–20518.
[11] K. Lu, et al., A rechargeable iodine-carbon battery that exploits ion intercalation and iodine redox chemistry, Nat. Commun. 8 (2017) 527.
[12] X. Dong, et al., Environmentally-friendly aqueous Li (or Na)-ion battery with fast electrode kinetics and super-long life, Sci. Adv. 2 (2016) e1501038.
[13] Z. Liu, et al., An ab initio study for probing iodization reactions on metallic anode surfaces of Li–I 2 batteries, J. Mater. Chem. A 6 (2018) 7807–7814.
[14] J. Liu, et al., Rational design of atomic-layer-deposited Lifepo4 as a high-performance cathode for lithium-ion batteries, Adv. Mater. 26 (2014) 6472–6477.
[15] H. Chen, et al., Rational design of cathode structure for high rate performance lithium–sulfur batteries, Nano Lett. 15 (2015) 5443–5448.
[16] Z. Su, et al., Robust pseudo-capacitive Li-I2 battery enabled by catalytic, adsorptive N-doped graphene interlayer, Energy Storage Mater. 14 (2018) 129–135.
[17] S. Kim, et al., Reduced graphene oxide/LiI composite lithium ion battery cathodes, Nano Lett. 17 (2017) 6893–6899.
[18] Z. Wu, et al., LiI Embedded meso-micro porous carbon polyhedrons for lithium iodine battery with superior lithium storage properties, Energy Storage Mater. 10 (2018) 62–68.
[19] Y. Yang, et al., High-capacity micrometer-sized Li2s particles as cathode materials for advanced rechargeable lithium-ion batteries, J. Am. Chem. Soc. 134 (2012) 15387–15394.
[20] K. Zhang, et al., Ultrasmall Li2S nanoparticles anchored in graphene nanosheets for high-energy lithium-ion batteries, Sci. Rep. 4 (2014) 6467.
[21] C. Hu, et al., Alleviating polarization by designing ultrasmall Li2S nanocrystals encapsulated in N-rich carbon as a cathode material for high-capacity, long-life Li-S batteries, J. Mater. Chem. A 4 (2016) 18284–18288.
[22] A. Luntz, et al., Tunneling and polaron charge transport through Li2o2 in Li–O2 batteries, J. Phys. Chem. Lett. 4 (2013) 3494–3499.
[23] M.D. Radin, C.W. Monroe, D.J. Siegel, Impact of space-charge layers on sudden death in Li/O2 batteries, J. Phys. Chem. Lett. 6 (2015) 3017–3022.
[24] Q. Zhang, et al., Understanding the anchoring effect of two-dimensional layered materials for lithium–sulfur batteries, Nano Lett. 15 (2015) 3780–3786.
[25] Z. Liu, P.B. Balbuena, P.P. Mukherjee, Mesoscale evaluation of titanium silicide monolayer as a cathode host material in lithium–sulfur batteries, JOM 69 (2017) 1532–1536.
[26] Z. Liu, P.B. Balbuena, P.P. Mukherjee, Evaluating silicene as a potential cathode host to immobilize polysulfides in lithium–sulfur batteries, J. Coord. Chem. 69 (2016) 2090–2105.
[27] L. Zhang, et al., Borophene as efficient sulfur hosts for lithium–sulfur batteries: suppressing shuttle effect and improving conductivity, J. Phys. Chem. C 121 (2017) 15549–15555.
[28] F. Li, J. Zhao, Atomic sulfur anchored on silicene, phosphorene, and borophene for excellent cycle performance of Li–S batteries, ACS Appl. Mater. Interfaces 9 (2017) 42836–42844.
[29] Y. Qie, et al., C_3B monolayer as an anchoring material for lithium-sulfur batteries, Carbon 129 (2018) 38–44.
[30] Z. Liu, P.B. Balbuena, P.P. Mukherjee, Revealing charge transport mechanisms in Li2S2 for Li–sulfur batteries, J. Phys. Chem. Lett. 8 (2017) 1324–1330.
[31] H. Wang, et al., Tailored reaction route by micropore confinement for Li–S batteries operating under lean electrolyte conditions, Adv. Energy Mater. (2018) 1800590.
[32] F. Tian, M.D. Radin, D.J. Siegel, Enhanced charge transport in amorphous Li2O2, Chem. Mater. 26 (2014) 2952–2959.
[33] Y.L. Zhang, et al., Amorphous Li2o2: chemical synthesis and electrochemical properties, Angew. Chem.-Int. Ed. 55 (2016) 10717–10721.
[34] M.J. Klein, G.M. Veith, A. Manthiram, Chemistry of sputter-deposited lithium sulfide films, J. Am. Chem. Soc. 139 (2017) 10669–10676.
[35] Z. Liu, et al., Revealing reaction mechanisms of nanoconfined Li2S: implications for lithium-sulfur batteries, Phys. Chem. Chem. Phys. 20 (2018) 11713–11721.
[36] T. Yu, et al., Understanding the role of lithium sulfide clusters in lithium-sulfur batteries, J. Mater. Chem. A 5 (2017) 9293–9298.
[37] M. Yin, M.L. Cohen, Theoretical determination of surface atomic geometry: si (001)-(2× 1), Phys. Rev. B 24 (1981) 2303.
[38] H. Ott, Die Raumgitter Der Lithiumhalogenide, Phys. Z. 24 (1923) 209–213.
[39] M. Yu, D.R. Trinkle, Accurate and efficient algorithm for bader charge integration, J. Chem. Phys. 134 (2011) 064111.
[40] W. Tang, E. Sanville, G. Henkelman, A grid-based bader analysis algorithm without lattice bias, J. Phys.-Condens. Matter 21 (2009) 084204.
[41] Y. Zhao, et al., A 3.5 V lithium–iodine hybrid redox battery with vertically aligned carbon nanotube current collector, Nano Lett. 14 (2014) 1085–1092.
[42] D. Gong, et al., An iodine quantum dots based rechargeable sodium–iodine battery, Adv. Energy Mater. 7 (2017) 1601885.
[43] K. Lu, et al., Rechargeable potassium-ion batteries enabled by potassium-iodine conversion chemistry, Energy Storage Mater. 16 (2019) 1–5.
[44] H. Tian, et al., High power rechargeable magnesium/iodine battery chemistry, Nat. Commun. 8 (2017) 14083.
[45] F. Bertasi, et al., Toward a magnesium-iodine battery, Adv. Funct. Mater. 26 (2016) 4860–4865.
[46] H. Pan, et al., Controlling solid–liquid conversion reactions for a highly reversible aqueous zinc–iodine battery, ACS Energy Lett. 2 (2017) 2674–2680.
[47] H. Tian, et al., Rechargeable aluminum/iodine battery redox chemistry in ionic liquid electrolyte, ACS Energy Lett. 2 (2017) 1170–1176.
[48] L. Visscher, K. Dyall, Relativistic and correlation effects on molecular properties. I. The dihalogens F2, Cl2, Br2, I2, and At2, J. Chem. Phys. 104 (1996) 9040–9046.
[49] G.L. Miessler, D.A. Tarr, Inorganic Chemistry, Pearson Education, Upper Saddle River, NJ, 2004, p. 345.
[50] A. Hazell, Unit-cell dimensions of thallous tri-iodide, Acta Crystallogr. 16 (1963) (71-71).
[51] R. Thomas, F. Moore, Neutron diffraction studies of polyiodides. I. Potassium triiodide monohydrate, Acta Crystallogr. Sect. B: Struct. Crystallogr. Cryst. Chem. 36 (1980) 2869–2873.
[52] Z. Meng, et al., Polyiodide-shuttle restricting polymer cathode for rechargeable lithium/iodine battery with ultralong cycle life, ACS Appl. Mater. Interfaces 10 (2018) 17933–17941.
[53] L. Zhang, et al., Revealing the electrochemical charging mechanism of nanosized Li2s by in situ and operando x-ray absorption spectroscopy, Nano Lett. 17 (2017) 5084–5091.
[54] Y.-X. Chen, P. Kaghazchi, Metalization of Li2S particle surfaces in Li–S batteries, Nanoscale 6 (2014) 13391–13395.
[55] M.D. Radin, et al., Lithium peroxide surfaces are metallic, while lithium oxide surfaces are not, J. Am. Chem. Soc. 134 (2011) 1093–1103.
[56] A. Fonari, S. Stauffer, Vasp_Raman.Py, 2013. ⟨https://github.com/raman-sc/VASP/⟩.
[57] E.M. Nour, L.H. Chen, J. Laane, Far-infrared and Raman spectroscopic studies of polyiodides, J. Phys. Chem. 90 (1986) 2841–2846.
[58] A. Van der Ven, et al., First-principles investigation of phase stability in ${/Mathrm{Li}}_{X}{/Mathrm{Coo}}_{2}$, Phys. Rev. B 58 (1998) 2975–2987.
[59] G. Yang, et al., Insight into the role of Li2s2 in Li-S batteries: a first-principles study, J. Mater. Chem. A 3 (2015) 8865–8869.
[60] M.K. Aydinol, et al., Ab initio study of lithium intercalation in metal oxides and metal dichalcogenides, Phys. Rev. B 56 (1997) 1354–1365.
[61] D. Moy, A. Manivannan, S. Narayanan, Direct measurement of polysulfide shuttle current: a window into understanding the performance of lithium-sulfur cells, J. Electrochem. Soc. 162 (2015) A1–A7.
[62] C. Barchasz, et al., Lithium/sulfur cell discharge mechanism: an original approach for intermediate species identification, Anal. Chem. 84 (2012) 3973–3980.
[63] M.A. Lowe, J. Gao, H.D. Abruña, Mechanistic insights into operational lithium–sulfur batteries by in situ x-ray diffraction and absorption spectroscopy, Rsc Adv. 4 (2014) 18347–18353.
[64] M. Cuisinier, et al., Sulfur speciation in Li–S batteries determined by operando x-ray absorption spectroscopy, J. Phys. Chem. Lett. 4 (2013) 3227–3232.
[65] G. Hautier, et al., Phosphates as lithium-ion battery cathodes: an evaluation based on high-throughput ab initio calculations, Chem. Mater. 23 (2011) 3495–3508.
[66] L. de Biasi, et al., Between scylla and charybdis: balancing among structural stability and energy density of layered Ncm cathode materials for advanced lithium-ion batteries, J. Phys. Chem. C 121 (2017) 26163–26171.
[67] M. Wild, et al., Lithium sulfur batteries, a mechanistic review, Energy Environ. Sci. 8 (2015) 3477–3494.
[68] X. Meng, et al., Vapor-phase atomic-controllable growth of amorphous Li2s for high-performance lithium-sulfur batteries, Acs Nano 8 (2014) 10963–10972.
[69] S. Xin, et al., Smaller sulfur molecules promise better lithium–sulfur batteries, J. Am. Chem. Soc. 134 (2012) 18510–18513.
[70] Z. Liu, P.B. Balbuena, P.P. Mukherjee, Hole polaron diffusion in the final discharge product of lithium–sulfur batteries, J. Phys. Chem. C 121 (2017) 17169–17175.
[71] J. Garcia-Lastra, et al., Dft+ U study of polaronic conduction in Li2O2 and Li2CO3: implications for Li–Air batteries, J. Phys. Chem. C 117 (2013) 5568–5577.
[72] S. Li, J. Liu, B. Liu, First-principles study of the charge transport mechanisms in lithium superoxide, Chem. Mater. 29 (2017) 2202–2210.
[73] S.P. Ong, Y. Mo, G. Ceder, Low hole polaron migration barrier in lithium peroxide, Phys. Rev. B 85 (2012) 081105.
[74] M.D. Radin, C.W. Monroe, D.J. Siegel, How dopants can enhance charge transport in Li2O2, Chem. Mater. 27 (2015) 839–847.
[75] R.B. Araujo, S. Chakraborty, R. Ahuja, Unveiling the charge migration mechanism in Na2O2: implications for sodium–air batteries, Phys. Chem. Chem. Phys. 17 (2015) 8203–8209.
[76] S. Yang, D.J. Siegel, Intrinsic conductivity in sodium–air battery discharge phases: sodium superoxide vs sodium peroxide, Chem. Mater. 27 (2015) 3852–3860.
[77] J.G. Smith, et al., Intrinsic conductivity in magnesium–oxygen battery discharge products: Mgo and Mgo2, Chem. Mater. 29 (2017) 3152–3163.
[78] H. Park, et al., Adiabatic and nonadiabatic charge transport in Li–S batteries, Chem. Mater. 30 (2018) 915–928.
[79] A.C. Luntz, et al., Tunneling and polaron charge transport through Li2o2 in Li–O2

batteries, J. Phys. Chem. Lett. 4 (2013) 3494–3499.
[80] A.V. Krukau, et al., Influence of the exchange screening parameter on the performance of screened hybrid functionals, J. Chem. Phys. 125 (2006) 224106.
[81] J. Varley, et al., Lithium and oxygen vacancies and their role in Li2O2 charge transport in Li–O2 batteries, Energy Environ. Sci. 7 (2014) 720–727.
[82] Z. Zhang, et al., Selenium/carbon-rich core–shell composites as cathode materials for rechargeable lithium–selenium batteries, J. Power Sources 279 (2015) 88–93.
[83] G. Li, et al., Giant Raman response to the encapsulation of sulfur in narrow diameter single-walled carbon nanotubes, J. Am. Chem. Soc. 138 (2015) 40–43.
[84] T. Fujimori, et al., Conducting linear chains of sulphur inside carbon nanotubes, Nat. Commun. 4 (2013) 2162.
[85] Y. Zhao, L. Wang, H.R. Byon, High-performance rechargeable lithium-iodine batteries using triiodide/iodide redox couples in an aqueous cathode, Nat. Commun. 4 (2013) 1896.
[86] G. Kresse, J. Furthmüller, Efficiency of ab-initio total energy calculations for metals and semiconductors using a plane-wave basis set, Comput. Mater. Sci. 6 (1996) 15–50.
[87] G. Kresse, J. Hafner, Ab initio, Phys. Rev. B 48 (1993) 13115–13118.
[88] R. Car, M. Parrinello, Unified approach for molecular dynamics and density-functional theory, Phys. Rev. Lett. 55 (1985) 2471–2474.
[89] R.O. Jones, O. Gunnarsson, The density functional formalism, its applications and prospects, Rev. Mod. Phys. 61 (1989) 689–746.
[90] P.E. Blöchl, Projector augmented-wave method, Phys. Rev. B 50 (1994) 17953–17979.
[91] J.P. Perdew, K. Burke, M. Ernzerhof, Generalized gradient approximation made simple, Phys. Rev. Lett. 77 (1996) 3865–3868.
[92] S. Nose, A unified formulation of the constant temperature molecular dynamics methods, J. Chem. Phys. 81 (1984) 511–519.